



Purification of Waste Silicon Powder Derived from Kerf Loss Slurry by Radial Directional Solidification and Comparison with Other Directional Solidification Practices

Minako Imose¹ · Daigo Araki² · Md. Azhar Uddin² · Yoshiei Kato² · Kiyoshi Kinoshita³

Received: 18 June 2021 / Accepted: 22 December 2021 / Published online: 17 January 2022
© The Minerals, Metals & Materials Society 2022

Abstract

Radial directional solidification, in which a liquid is solidified toward the radial center, was explored as a technique for recycling kerf loss silicon powder into SOG-Si. The purification behavior of the metallic impurities Fe, Al, Ca, Mg, Ti, Mn, and Ni was examined experimentally and numerically. Specific resistivity after solidification achieved a range of 0.00029 to 0.00075 Ωm and an average value of 0.0005 Ωm . From the calculation of the concentration and specific resistivity profiles of each element in the silicon sludge, specific resistivity was estimated to be determined by Fe and Ca. The Fe and Al concentration profiles in three different directional solidification practices were computed under the same solidification time and distance conditions. In radial directional solidification, Fe purification was promoted most strongly close to the solid fraction of 0.8 and then rapidly diminished. This purification behavior depended on the lower instantaneous solidification rate in the radial direction at the position before the solid fraction of 0.8 and was followed rapidly by a higher solidification rate. Al purification in the radial directional solidification practice was slightly different from that in longitudinal solidification due to the small difference in the effective distribution coefficient in this calculation situation.

The contributing editor for this article was Karl Bernhard Friedrich.

✉ Yoshiei Kato
y-kato@cc.okayama-u.ac.jp

Minako Imose
ev420409@s.okayama-u.ac.jp

Daigo Araki
pcgq3ixz@s.okayama-u.ac.jp

Md. Azhar Uddin
alazhar@cc.okayama-u.ac.jp

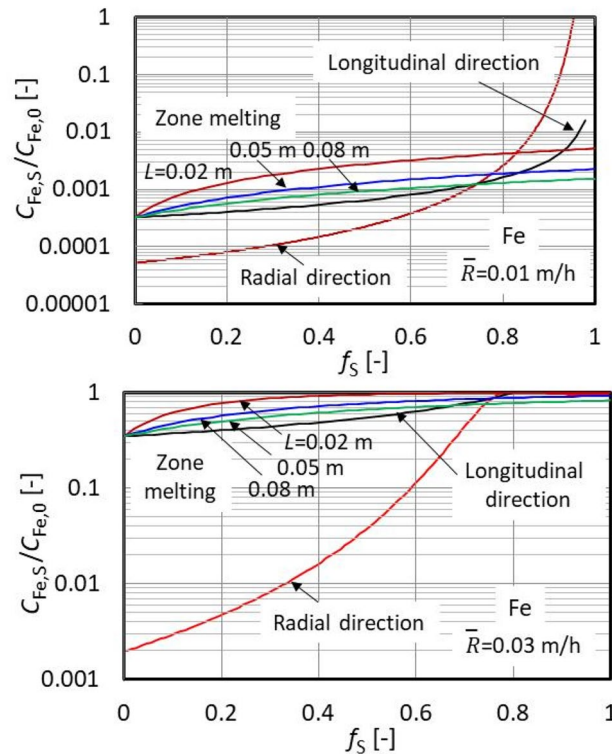
Kiyoshi Kinoshita
kinowrks@mint.ocn.ne.jp

¹ Department of Environmental Chemistry and Materials, Faculty of Environmental Science and Technology, Okayama University, 1-1 Tsushima-naka, 3-chome, Kita-ku, Okayama 700-8530, Japan

² Department of Material and Energy Science, Graduate School of Environmental and Life Science, Okayama University, 1-1 Tsushima-naka, 3-chome, Kita-ku, Okayama 700-8530, Japan

³ Kinoshita Manufactory Co., Ltd, 11-39 Ozu, 4-chome, Minami-ku, Hiroshima 732-0802, Japan

Graphical Abstract



Keywords Silicon sludge · Kerf loss · Directional solidification · Solar grade silicon

Introduction

Control of carbon dioxide emissions is one of the most effective measures for slowing global warming. From this viewpoint, solar photovoltaic (PV) power has attracted attention as a fossil fuel alternative, and installed PV capacity has increased rapidly since the end of the twentieth century. Since 80 to 90% of solar cells are made from crystalline silicon, it is important to reduce the environmental load and manufacturing cost of this material. According to Nakato et al. [1], only 0.13 kg of silicon wafer was produced from 1 kg of metallurgical-grade silicon (MG-Si), and the remainder was lost in the course of manufacturing solar grade silicon (SOG-Si) from MG-Si and the subsequent wafer production process. Waste in the wafer production process consists of scrapped SOG ingots after cutting, kerf loss silicon powder in the sawing process, defective or broken wafers, etc. [2]. Because both the wafer thickness and wire width have been reduced with advances in wafer technology, kerf loss silicon is now equivalent to more than 40% of the silicon ingot before sawing. Thus, it is important to reproduce SOG-Si from the sawing slurry, which contains high-purity silicon powder.

Recycling of kerf loss silicon waste has been reviewed by several researchers [2–6]. Many methods for separation and purification of silicon powder from kerf loss slurry exist, including physical separation of silicon, silicon carbide (SiC) and lubricating oil by phase transfer separation [7–9], centrifugation [10], supercritical water [11], chemical treatment by etching metallic impurities after SiC removal [12], silicon hydrobromination [13], metallurgical refining by slag extraction [14], and directional solidification [14–16]. In these practices, the ingot obtained by directional solidification can be moved to the sawing process while satisfying SOG-Si specifications.

This paper deals with the removal of metallic impurities by directional solidification of molten silicon powder after separating the SiC and lubricant oil contents in order to reproduce SOG-Si. Although many studies have investigated the directional solidification process as a technique for purifying MG-Si to SOG-Si [17–24] and have also provided detailed thermodynamic support [25–27], few have examined the differences among directional solidification methods.

As shown schematically in Fig. 1, there are three directional solidification methods, including methods in which

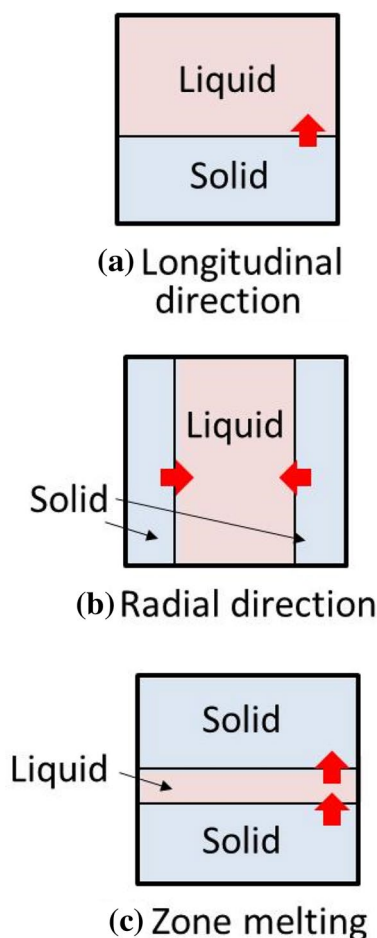


Fig. 1 Conceptual diagram of three directional solidification practices

the melting pool decreases with time [28] and solidification proceeds in either the longitudinal direction ((a) in Fig. 1) or radial direction ((b) in Fig. 1), and a method called “zone melting,” in which the melting pool is moved to a given position ((c) in Fig. 1) [29]. Radial directional solidification, in which the silicon melt is solidified toward the center in the radial direction, has not been discussed sufficiently in previous studies.

In this study, the purification behavior of kerf loss silicon powder was examined by radial directional solidification, and the three directional solidification practices of longitudinal solidification, radial solidification, and zone melting shown in Fig. 1 were compared by numerical analysis.

Experiment

The melting and solidification apparatus used in the radial directional solidification experiment was a vertical tubular furnace with a MoSi₂ heater (EF-6000, VF-1800-S, Crystal Systems Corporation), as shown schematically in Fig. 2.

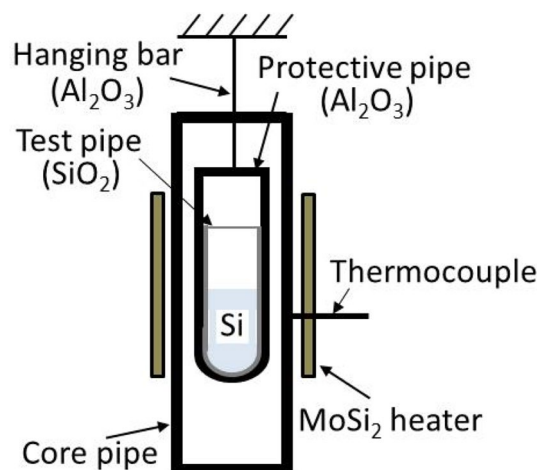


Fig. 2 Schematic diagram of apparatus used in radial directional solidification experiment

The silicon powder was charged to a height of 0.15 m in a SiO₂ test tube (inner diameter: 0.019 m, wall thickness: 0.002 m, height: 0.20 m) surrounded by an Al₂O₃ protective tube (inner diameter: 0.024 m, wall thickness: 0.003 m, height: 0.250 m). The sample tube was hung from an Al₂O₃ bar, and was then set in an Al₂O₃ furnace core tube (inner diameter: 0.050 m, wall thickness: 0.005 m, height: 0.90 m). A thermocouple was set in the center of the outer wall of the furnace core tube. The impurity composition is shown in Table 1.

The experiment was carried out under an argon atmosphere. The temperature was increased at a rate of 200 K/h, held at 1923 K in the center of the outer furnace core tube wall for 3 h for melting and then decreased at 200 K/h for solidification. The holding temperature was determined as a minimum temperature of complete melting of the sample. After cooling to room temperature, the sample was taken out and cut in the radial direction. The specific resistance of the cut plane was measured by a resistivity meter with a DC 4-point probe (K-705RS, Kyowa Riken Co., Ltd.).

Analysis of Purification in Directional Solidification

The temperature profiles of solid and liquid phases of metals are approximately flat when the thermal resistivity in the mold made from inorganic materials like SiO₂ and Al₂O₃ is a controlling factor in the latent heat transfer of solidification externally [30]. Moreover, as the silicon powder was partially melted for the holding temperature of Al₂O₃ core tube less than 1923 K in this experiment, the silicon temperature of the solid and liquid silicon was assumed to be kept at the melting point of silicon, T_m [K]. The heat and mass transfer

Table 1 Composition of silicon powder in experiment (Unit: mass %)

Si	Fe	Al	Ca	Mg	Ti	Mn	Ni
96.8	1.16	0.054	0.12	0.6	0.028	0.021	0.026

in radial directional solidification is shown schematically in Fig. 3. Heat transfer in the longitudinal direction is excluded. The temperature profiles of the SiO₂ and Al₂O₃ tubes, Ar atmosphere, and Al₂O₃ furnace core tube were schematically estimated based on their thermal conductivity values, although there were no experimental results. The heat of the silicon sample is removed to the right direction through the SiO₂ and Al₂O₃ tubes, argon atmosphere, and Al₂O₃ furnace core tube, whereas solidification proceeds in the opposite side so as to keep the heat balance between the latent heat generation and heat transfer rates. The heat balance equation of silicon is given by Eq. (1) from the fact that the released heat rate from the Al₂O₃ furnace core tube to the surroundings was kept to be 200 K/h.

$$\rho_{\text{Si}} \Delta H (-2\pi r_{\text{int}} \frac{dr_{\text{int}}}{dt}) = q, \quad (1)$$

where ρ_{Si} is the density of molten silicon ($= 2.57 \times 10^3 \text{ kg/m}^3$), ΔH is the latent heat of silicon solidification ($= 1.79 \times 10^6 \text{ J/kg}$), r_{int} is the solid/liquid interfacial radius [m], t is time [h], and q is the heat transfer rate per height [J/(h m)]. Equation (1) is solved under the condition that $r_{\text{int}} = r_{\text{in}}$ at $t = 0$, as follows:

$$r_{\text{int}} = \left(\left(-\frac{q}{\pi \rho_{\text{Si}} \Delta H} \right) t + r_{\text{in}}^2 \right)^{1/2}, \quad (2)$$

where r_{in} is the inner radius of the vessel [m].

The solid fraction, f_s [–], of silicon at r_{int} is as follows:

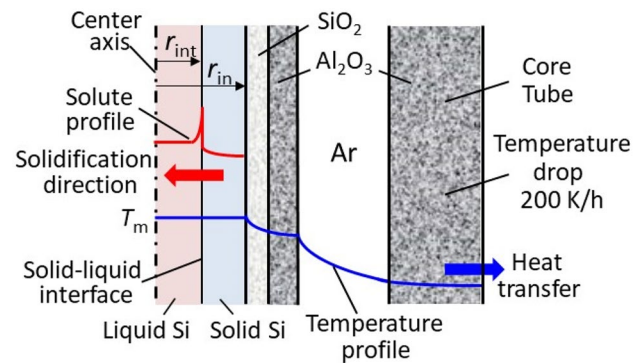
$$f_s = 1 - \left(\frac{r_{\text{int}}}{r_{\text{in}}} \right)^2 \quad (3)$$

The temporal changes in r_{int} and f_s are obtained from Eqs. (2) and (3) under a given q value. The solidification rate, R [m/h], is expressed by Eq. (4).

$$R = -\frac{dr_{\text{int}}}{dt} \quad (4)$$

The solidification rate ($=R$) in radial directional solidification changes with time and becomes larger at smaller r_{int} even if the heat transfer rate ($=q$) is constant, as indicated by Eq. (2).

When the impurities in silicon are assumed to have no diffusion in the solid phase, limited diffusion in the liquid phase near the solid/liquid interface and a perfectly mixed state in the liquid bulk phase, the solid concentration, $C_{i,s}$, of an impurity component i is expressed by Scheil's equation [28].

**Fig. 3** Schematic diagram of heat and mass transfer in radial directional solidification

$$C_{i,s} = k_{i,\text{eff}} C_{i,0} (1 - f_s)^{k_{i,\text{eff}} - 1}, \quad (5)$$

where $k_{i,\text{eff}}$ is the effective distribution coefficient of the i component [–] and $C_{i,0}$ is the initial concentration of the i component [mass ppm]. The $k_{i,\text{eff}}$ value is given by the following Burton's equation [31].

$$k_{i,\text{eff}} = \frac{k_{i,0}}{\left(k_{i,0} + (1 - k_{i,0}) \exp\left(-\frac{R\delta}{3600 D_{i,L}}\right) \right)}, \quad (6)$$

where $k_{i,0}$ is the equilibrium distribution coefficient [–], δ is the diffusion thickness in the liquid phase [m], and $D_{i,L}$ is the diffusion coefficient of the i component in the liquid phase [m²/s]. Yuge et al. [21] showed that the δ value was 0.004 m to explain the Fe purification behavior in molten silicon for a zone melting practice with a natural convection (no crucible rotation), and it was decreased with the increasing rotation speed of the crucible. Thus, δ of 0.004 m for all components was assumed to calculate the effective distribution coefficient due to no rotation in this condition. In the exponential term of Eq. [6], $\frac{R}{3600}$ [m/s] was used for matching the unit of $\frac{\delta}{D_{i,L}}$ [m/s]. Substituting Eq. (6) into Eq. (5) with the own physical property of each component, $C_{i,s}$ is calculated for each f_s and r_{int} value.

In longitudinal directional solidification, the cross-sectional area of the solid/liquid interface generally remains unchanged, as shown in Fig. 1, which leads to the relationship between f_s [–] and the height, Z_{int} [m], of the solid/liquid interface instead of Eq. (3) as follows:

$$f_s = \frac{Z_{\text{int}}}{Z_0}, \quad (7)$$

where Z_0 is the height at perfect solidification [m]. As in the case of radial directional solidification, Eqs. (5) and (6) are obtained on the assumptions of no diffusion in the solid phase, limited diffusion in the liquid phase near the solid/liquid interface and a perfectly mixed state in the liquid bulk phase.

In zone melting, the constant cross-sectional area of the solid/liquid interface leads to Eq. (7), and the same assumptions regarding solid and liquid diffusion as in the radial and longitudinal directional solidification practices make it possible to describe $C_{i,s}$ by Pfann's equation [29], as follows:

$$C_{i,s} = C_{i,0} \left(1 - (1 - k_{i,\text{eff}}) \exp \left(-\frac{k_{i,\text{eff}} Z_{\text{int}}}{L} \right) \right), \quad (8)$$

where L is the melting pool thickness [m].

Thus, in the purification behavior of molten silicon in the three directional solidification practices described above, the solidification rates of longitudinal directional solidification and zone melting were constant for a fixed heat transfer rate, whereas that of radial directional solidification increased, especially at the end of solidification, that is, near the central axis.

Results and Discussion

Radial Directional Solidification

As the temperature of the furnace core tube decreases at the rate of 200 K/h, the heat transfer rate, q [J/m h], in this experiment is obtained from

$$q = \rho_{\text{Al}_2\text{O}_3} S C_p (200) = (3.9 \times 10^3) (8.64 \times 10^{-4}) (1.32 \times 10^3) (200) = 8.90 \times 10^5 \frac{\text{J}}{\text{mh}}, \quad (9)$$

where $\rho_{\text{Al}_2\text{O}_3}$, S , and C_p are the density of Al_2O_3 ($= 3.9 \times 10^3 \text{ kg/m}^3$), the cross-sectional area ($= 8.64 \times 10^{-4}$), and the specific heat at a constant pressure and 1500 K ($= 1.32 \times 10^3 \text{ J/(kg K)}$) of the furnace core tube, respectively.

$r_{\text{int}}/r_{\text{in}}$ is calculated by substituting the q value from Eq. (9) into Eq. (2), and f_s is then obtained from Eq. (3). The relationship between $r_{\text{int}}/r_{\text{in}}$, f_s , and t is shown in Fig. 4. The solid fraction increased in proportion to the solidification time, whereas the radius of the solid/liquid interface decreased slowly in the initial and middle solidification periods and then declined drastically approaching the end of solidification. From the temporal change in $r_{\text{int}}/r_{\text{in}}$, the solidification rate, R , was estimated to increase rapidly in the final stage of solidification.

The equilibrium distribution coefficient, $k_{i,0}$ [–], and diffusion coefficient, $D_{i,L}$ [m^2/s], of the impurities in molten

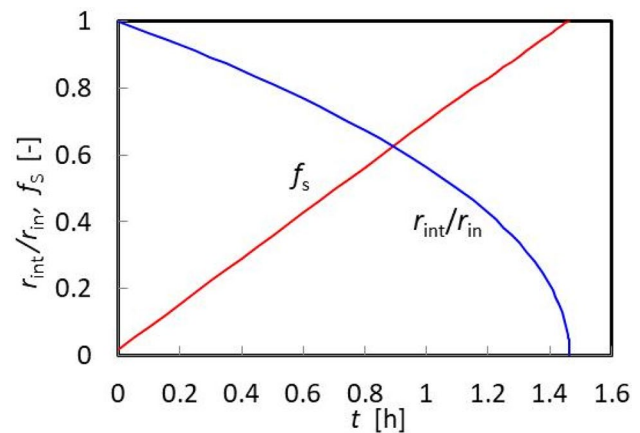


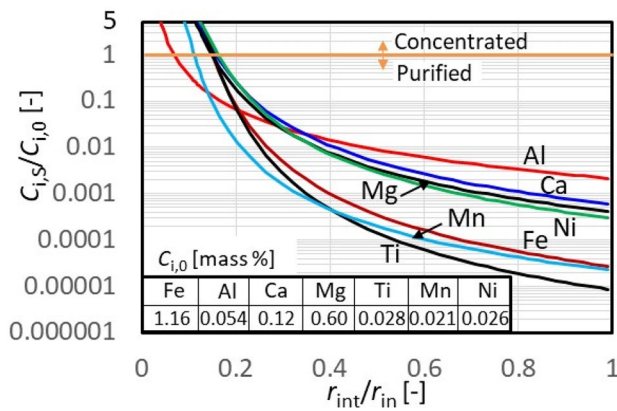
Fig. 4 Calculated temporal changes of mass fraction and interfacial radius of solid and liquid

silicon used in the calculation are shown in Table 2. The $k_{i,0}$ according to Trumbore [32] was adopted for Fe, Al, Mn, and Ni, the value according to Hopkins et al. [33] was used for Ti, and the values given by Kawanishi and Yoshikawa [34] were used for Ca and Mg. The values given by Tang et al. [35] were used for the $D_{i,L}$ of Fe, Al, Ti, Mn, and Ni. Safarian and Tangstad [36] calculated the $D_{i,L}$ values of Ca and Mg to be 1.51×10^{-8} and $2.1 \times 10^{-8} \text{ m}^2/\text{s}$, respectively, by the use of the modified Stocks–Einstein equation. However, as these values were untested by the experimental data, we assumed the $D_{i,L}$ of Ca and Mg to be $1 \times 10^{-8} \text{ m}^2/\text{s}$ in this case. The calculated solid concentration profiles of the metallic impurities are shown in Fig. 5. The $r_{\text{int}}/r_{\text{in}}$ values of 1 and 0 indicate the start and end of solidification, respectively. $C_{i,s}/C_{i,0} < 1$ means that an impurity component i is purified, whereas $C_{i,s}/C_{i,0} > 1$ represents that it is concentrated. The range of $C_{i,s}/C_{i,0} \leq 5$ is shown in Fig. 5 because the larger $C_{i,s}/C_{i,0}$ values at smaller $r_{\text{int}}/r_{\text{in}}$ were unstably calculated due to excess R of Eq. (4) and rapid drop of $r_{\text{int}}/r_{\text{in}}$ in Fig. 4. During purification, each impurity concentration increased with the decrease in $r_{\text{int}}/r_{\text{in}}$, and purification came to a stop at $r_{\text{int}}/r_{\text{in}} < 0.2$ due to impurity condensation and the rapid increase in the solidification rate, as shown in Fig. 4. In the early and middle stages of solidification, $C_{i,s}/C_{i,0}$ decreased with the decrease in $k_{i,0}$ in Table 2. The largest $k_{i,0}$ and $D_{i,L}$ of Al in Table 2 resulted in the highest Al concentration at the early and middle stages of solidification and a relatively lower concentration in the final stage.

The specific resistance of an arbitrary spot on the sample cut plane was measured twenty times, excluding the area of $0.3r_{\text{in}}$ in the radius. The relationship between the specific resistivity and trial number is shown in Fig. 6. The specific resistivity values ranged from 2.9×10^{-4} to $7.5 \times 10^{-4} \Omega\text{m}$, and the average value was $5.0 \times 10^{-4} \Omega\text{m}$. It was about

Table 2 Equilibrium distribution coefficient and diffusivity of impurities

	Fe	Al	Ca	Mg	Ti	Mn	Ni
$k_{i,0}$ [-]	8×10^{-6}	2×10^{-3}	2.9×10^{-4}	2.1×10^{-4}	2×10^{-6}	1×10^{-5}	1.2×10^{-4}
$D_{i,L}$ [m ² /s]	3×10^{-9}	6×10^{-8}	1×10^{-8}	1×10^{-8}	2.5×10^{-9}	4.5×10^{-9}	4×10^{-9}

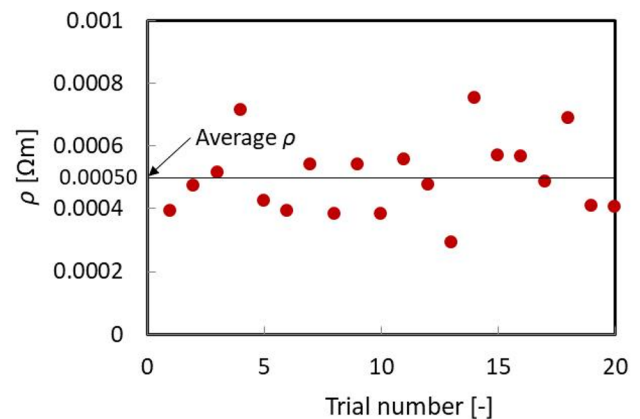
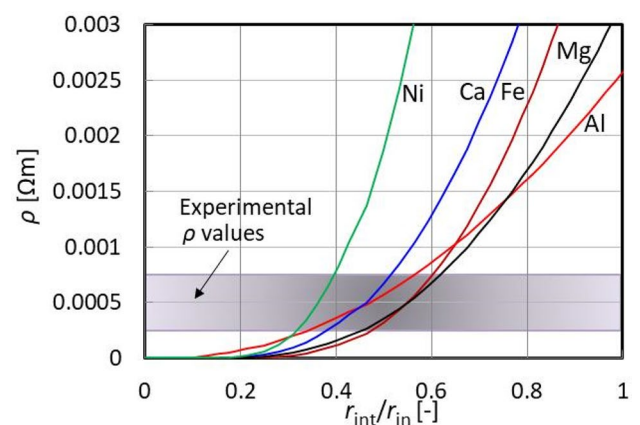
**Fig. 5** Calculated solid concentration profiles of impurities

one-twentieth the average resistivity obtained by Kato et al. [19] and Yuge et al. [20] who refined metallurgical-grade silicon to SOG-Si by a metallurgical purification process with two directional solidification practices. Thus, further solidification purification is required for SOG-Si.

It is essentially difficult to predict the electrical resistivity from the impurity concentration because carrier orbit should be greatly affected by impurities, the activation rate from each component must be considered, and acceptors and donors may be compensated, etc. Here, a simplified equation of the electrical resistivity was used. The number concentration, C_i^* , of the impurity component i [m⁻³], the electron or hole mobility, μ [m²/(V s)], and the specific electrical resistivity, ρ [Ω m], are interrelated, as shown by the following equation [37].

$$\rho = \frac{1}{C_i^* q_C \mu}, \quad (10)$$

where q_C is the electric charge [C]. As Fe and Ni are N-type impurities and Al, Ca, and Mg are P-type impurities, the values of μ are 0.16 and 0.04 [m²/(V s)], respectively [37]. The specific resistivities of Fe, Al, Ca, Mg, and Ni, which form a higher $C_{i,s}/C_{i,0}$ group in Fig. 5, were calculated by Eq. (10) and compared with the experimental results shown in Fig. 7. The calculated ρ curves decreased with decreasing r_{int}/r_{in} due to the larger $C_{i,s}/C_{i,0}$ values. Assuming that the experimental ρ corresponds to the minimum ρ in the metallic impurities, the elements Fe and Ca determined the ρ values

**Fig. 6** Relationship between specific resistivity value and trial number**Fig. 7** Comparison of solid concentration dependency and specific resistivity in experiment and calculation for each impurity

in this experiment, and the range of r_{int}/r_{in} was between 0.49 and 0.62. Therefore, contamination control of these elements is important for effectively purifying kerf loss silicon powder. The ρ curve of Al indicated the minimum in the first stage of solidification until r_{int}/r_{in} reached 0.8 because Al had the highest equilibrium distribution coefficient and decreased with the decreasing r_{int}/r_{in} . However, with the progress of solidification, it became relatively higher than the ρ curves of the other impurities as a result of the larger D_{Al} and smaller $C_{Al,0}$ values.

Comparison of Calculated Silicon Purification in Three Directional Solidification Practices

The purification behaviors of silicon in the three directional solidification practices described above were calculated and compared under the same solidification conditions. The radius in radial directional solidification and the height in longitudinal directional solidification and zone melting were fixed at 0.3 m. The solidification times of 10 and 30 h were used for the calculation, corresponding to the average solidification rates of 0.01 and 0.03 m/h, respectively. The liquid pool thickness in zone melting was changed to 0.02, 0.05 or 0.08 m. Because the kerf loss silicon powder is obtained from cutting silicon ingot by steel wire saw and Al has the highest equilibrium distribution coefficient in Table 2, Fe and Al were used in the calculation as typical impurities.

The comparison of the change in Fe purification in the three directional solidification practices is shown in Fig. 8. Here, although both radial and longitudinal solidification practices have $C_{Fe,S}/C_{Fe,0} > 1$ for $f_s \rightarrow 0$ as is the case with Fig. 5, the range of $C_{Fe,S}/C_{Fe,0} < 1$ was chosen in Fig. 8 due to the focus of Fe purification. The upper and lower figures indicate the conditions of the average solidification rates of 0.01 m/h and 0.03 m/h, respectively. At both solidification rates, the $C_{Fe,S}$ in radial directional solidification was the lowest among the three practices at $f_s < 0.8$ and conversely became the highest at $f_s > 0.8$. Longitudinal directional solidification showed the second highest purification capacity at $f_s < 0.8$, but the $C_{Fe,S}$ curve was larger than that of zone melting. In zone melting, the Fe concentration remained relatively unchanged in spite of having the largest values at $f_s < 0.8$, and Fe purification decreased with a decreasing liquid pool thickness. The relationship between the solidification rate, $-dr_{int}/dt$, mass fraction of solid, f_s , and radius, r_{int}/r_{in} , of the liquid/solid interface in radial directional solidification is shown in Fig. 9, where solidification proceeds in the direction of smaller r_{int} . The instantaneous solidification rate became smaller than the average rate close to $f_s = 0.8$. In other words, the solidification rate in radial directional solidification was the smallest among the three directional solidification practices at $f_s < 0.8$, which was caused by the small $k_{Fe,eff}$ and $C_{Fe,S}$ values, as indicated in Eqs. (5), (6) and (8).

As in the comparison of Fe in Fig. 8, the calculated Al purification behavior was compared for the three directional solidification practices, as shown in Fig. 10. Although the same purification trend as in the case of Fe was recognized in the three directional solidification practices, the difference between the radial and longitudinal solidification practices was significantly small because the diffusivity coefficient of Al is larger than that of Fe, which reduces the exponential term in Eq. (6) to close to zero and thus diminishes the difference of $k_{Al,eff}$.

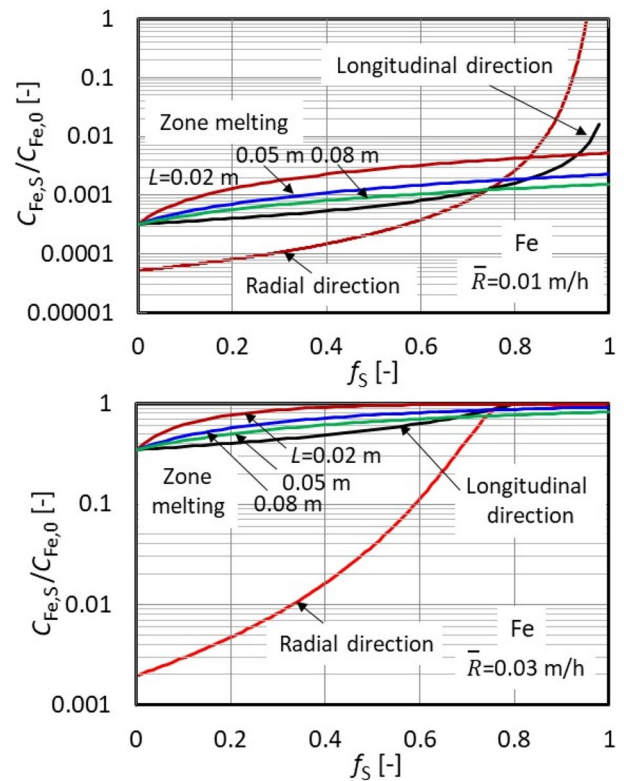


Fig. 8 Comparison of Fe purification in three directional solidification practices

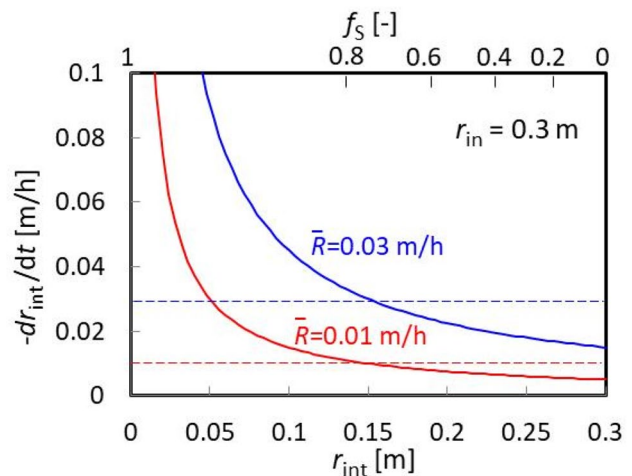


Fig. 9 Relationship between solidification rate, mass fraction of solid, and radius of liquid–solid interface in radial directional solidification

Radial directional solidification is effective as a silicon purification practice, especially for elements which are easily affected by the solidification rate, because it is possible to maintain a smaller solidification speed until the solid fraction ratio reaches approximately 0.8. The use of radial directional solidification as the first step solidification purification

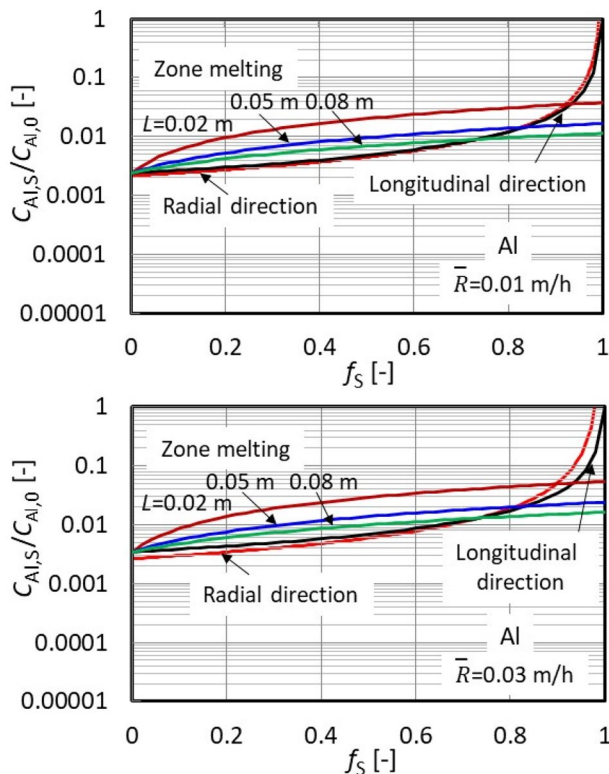


Fig. 10 Comparison of Al purification in three directional solidification practices

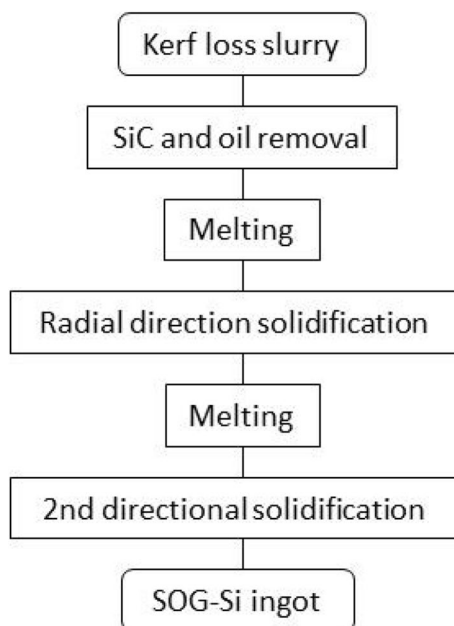


Fig. 11 Example of purification process of kerf loss silicon by radial directional solidification

process is preferable, as this practice eliminates the impurity condensation zone around the ingot center, which makes application to SOG-Si ingots difficult. In this manner, a process flow for SOG-Si manufacturing using kerf loss silicon slurry as a feedstock is shown in Fig. 11, where the first- and second-step solidification practices are performed.

Conclusions

The purification behavior of kerf loss silicon powder was examined by radial directional solidification and was compared numerically in the three directional solidification practices of radial solidification, longitudinal solidification, and zone melting.

- (1) The metallic impurities Fe, Al, Ca, Mg, Ti, Mn, and Ni in the silicon sludge powder were purified by radial directional solidification, and the specific resistivity after purification achieved a range of 0.00029 to 0.00075 Ωm and an average value of 0.0005 Ωm . From the calculation of the concentration and specific resistivity profiles of each element in the silicon sludge, specific resistivity was estimated to be determined by Fe and Ca in this experiment.
- (2) The Fe and Al concentration profiles were calculated by setting equal solidification time and distance conditions for the three directional solidification practices. Fe purification in radial directional solidification was promoted most strongly close to the solid fraction of 0.8 and then rapidly diminished. This behavior depends on the lower instantaneous solidification rate at the radial directional position before the solid fraction of 0.8 and is followed rapidly by a higher solidification rate. Al purification in the radial directional solidification practice was slightly different from that in longitudinal solidification due to the small difference in the effective distribution coefficient in this calculation situation.

Funding This study was funded by Chugoku Bureau of Economy, Trade and Industry, Ministry of Economy, Trade, and Industry (METI Chugoku, H23).

Declarations

Conflict of interest The authors declare that they have no conflict of interest.

References

1. Nakato H, Nitta M, Uchimura R, Iinuma H, Uesugi H (2003) Investigation of characteristics and pretreatment method of high

- purity silicon sludge filtrated from wastewater of silicon industry (reuse technology of high purity silicon sludge—part I). *J Jpn Inst Met Mater* 67(10):562–568
2. Hachichi K, Lami A, Zemmouri H, Cuellar P, Soni R, Ait-Amar H, Drouiche N (2018) Silicon recovery from kerf slurry waste: a review of current status and perspective. *SILICON* 10:1579–1589
 3. Drouiche N, Cuellar P, Kerkar F, Medjahed S, Boutouchent-Guerfi N, Hamou MO (2014) Recovery of solar grade silicon from kerf loss slurry waste. *Renew Sust Energy Rev* 32:936–943
 4. Murthy HSGK (2015) Evolution and present status of silicon carbide slurry recovery in silicon wire sawing. *Resour Conserv Recycl* 104(Part A):194–205
 5. Wei K, Yang S, Wan X, Ma W, Wu J, Lei Y (2020) Review of silicon recovery and purification from saw silicon powder. *JOM* 72(7):2633–2647
 6. Li J, Lin Y, Wang F, Shi J, Sun J, Sun J, Ban B, Liu G, Chen J (2021) Progress in recovery and recycling of kerf loss silicon waste in photovoltaic industry. *Sep Purif Technol* 254:117581
 7. Shibata J, Murayama N, Nagae K (2006) Flotation separation of SiC from wastes in the silicon wafer slicing process. *Kagaku Kogaku Ronbunshu* 32(1):93–98
 8. Hsu HP, Huang WP, Yang CF, Lan CW (2014) Silicon recovery from cutting slurry by phase transfer separation. *Sep Purif Technol* 133:1–7
 9. Li DG, Xing PF, Zhuang YX, Li F, Tu GF (2014) Recovery of high purity silicon from SoG crystalline silicon cutting slurry waste. *Trans Nonferrous Met Soc China* 24:1237–1241
 10. Liu S, Huang K, Zhu H (2013) Recovery of silicon powder from silicon wire sawing slurries by tuning the particle surface potential combined with centrifugation. *Sep Purif Technol* 118:484–454
 11. Yoko A, Oshima Y (2013) Recovery of silicon from silicon sludge using supercritical water. *J Supercrit Fluids* 75:1–5
 12. Jang HD, Kim H, Kil DC, Chang H (2013) A novel recovery of silicon nanoparticles from a waste silicon sludge. *J Nanosci Nanotechnol* 13(3):2334–2338
 13. Tomono K, Miyamoto S, Ogawa T, Furuya H, Okamura Y, Yoshimoto M, Komatsu R, Nakayama M (2013) Recycling of kerf loss silicon derived from diamond-wire sawing cutting process by chemical approach. *Sep Purif Technol* 120:304–309
 14. Li X, Wu J, Xu M, Ma W (2019) Separation and purification of silicon from cutting kerf-loss slurry waste by electromagnetic and slag treatment technology. *J Clean Prod* 211:695–703
 15. Nakato H, Nitta M (2006) Reuse technology of high purity silicon sludge. *Seimitsu Kogaku Kaishi* 72(5):573–577
 16. Wang TY, Lin YC, Tai CY, Fei CC, Tseng MY, Lan CW (2009) Recovery of silicon from kerf loss slurry waste for photovoltaic applications. *Prog Photovolt Res Appl* 17:155–163
 17. Yuge N, Baba H, Sakaguchi Y, Nishikawa K, Terashima H, Aratani F (1994) Purification of metallurgical silicon up to solar grade. *Sol Energy Mater Sol Cells* 34:243–250
 18. Yuge N, Baba H, Sakaguchi Y, Terashima H, Aratani F (1997) Purification of silicon by directional solidification. *J Jpn Inst Met* 61(10):1094–1100
 19. Kato Y, Hanazawa K, Baba H, Nakamura N, Yuge N, Sakaguchi Y, Hiwasa S, Aratani F (2000) Purification of metallurgical grade silicon to solar grade for use in solar cell wafers. *Tetsu-to-Hagane* 86:717–724
 20. Yuge N, Abe M, Hanazawa K, Baba H, Nakamura N, Kato Y, Sakaguchi Y, Hiwasa S, Aratani F (2001) Purification of metallurgical-grade silicon up to solar grade. *Prog Photovolt Res Appl* 9:203–209
 21. Yuge N, Hanazawa K, Kato Y (2004) Removal of metal impurities in molten silicon by directional solidification with electron beam heating. *Mater Trans* 45:850–857
 22. Martorano MA, Ferreira Neto JB, Oliveira TS, Tsubaki TO (2011) Refining of metallurgical silicon by directional solidification. *Mater Sci Eng A* 176:217–226
 23. Liu T, Dong Z, Zhao Y, Wang J, Chen T, Xie H, Li J, Ni H, Huo D (2012) Purification of metallurgical silicon through directional solidification in a large cold crucible. *J Cryst Growth* 355(1):145–150
 24. Cablea M, Zaidat K, Gagnoud A, Nouri A, Delannoy Y (2014) Directional solidification of silicon under the influence of traveling magnetic field. *J Cryst Growth* 401:883–887
 25. Morita K, Miki T (2003) Thermodynamics of solar-grade-silicon refining. *Intermetallics* 11:1111–1117
 26. Yoshikawa T, Morita K, Kawanishi S, Tanaka T (2010) Thermodynamics of impurity elements in solid silicon. *J Alloys Compd* 490:31–41
 27. Morita K, Yoshikawa T (2011) Thermodynamic evaluation of new metallurgical refining processes for SOG-silicon production. *Trans Nonferrous Met Soc China* 21:685–690
 28. Sceil E (1942) Bemerkungen zur schichtkristallbildung. *Z Metallkd* 34:70–72
 29. Pfann WG (1952) Principles of zone-melting. *Trans AIME* 194:747–753
 30. Suzuki T (2013) Kogi-5 Gyoko Kiso (Lecture-5 Introduction to solidification), Dai 39kai Tekko Kogaku Seminar Text—Seiko Course—(Steelmaking Course Text of No. 39 Iron and Steel Engineering Seminar). The Iron and Steel Institute of Japan
 31. Burton JA, Prim RC, Slichter WP (1953) The distribution of solute in crystals grown from the melt. Part I. *Theor J Chem Phys* 21(11):1987–1991
 32. Trumbore FA (1960) Solid solubilities of impurity elements in germanium and silicon. *Bell Syst Tech J* 39:205–233
 33. Kawanishi S, Yoshikawa T (2017) Reassessment of silicon solubilities and thermodynamic properties of magnesium and calcium in silicon. *Mater Trans* 58(3):450–452
 34. Hopkins RH, Rohatgi A (1986) Impurity effects in silicon for high efficiency solar cells. *J Cryst Growth* 75:67–79
 35. Tang K, EvJ O, Tranell G, Tangstad M (2009) Critical assessment of the impurity diffusivities in solid and liquid silicon. *JOM* 61(11):49–55
 36. Safarian J, Tangstad M (2012) Vacuum refining of molten silicon. *Metall Mater Trans B* 43B:1427–1445
 37. Aoki M (1973) Semiconductor physics and semiconductor devices (1) Introduction to semiconductor physics. Television 27(7):553–563

Publisher's Note Springer Nature remains neutral with regard to jurisdictional claims in published maps and institutional affiliations.